MEASUREMENT SCIENCE REVIEW, **21**, (2021), No. 6, 197-204

sciendo

ISSN 1335-8871

MEASUREMENT SCIENCE REVIEW

Journal homepage: https://content.sciendo.com

3D Measurement of Discontinuous Objects with Optimized Dual-frequency Grating Profilometry

Jun Che[1], Yanxia Sun[2], Xiaojun Jin[1], Yong Chen[1]

[1]College of Mechanical and Electronic Engineering, Nanjing Forestry University, No.159 Longpan Road, No., 210037, Nanjing, China, corresponding author: Prof. Yong Chen, chenyongjsnj@163.com
[2]School of Rail Transportation, Nanjing Vocational Institute of Transport Technology, No.629 Longmian Avenue Science Park, No., 211188, Nanjing, China

Three-dimensional profilometry tends to be less effective at measuring discontinuous surfaces. To overcome this problem, an optimized profilometry based on fringe projection is proposed in this paper. Due to the limitation of the shooting angle, there are projection blind spots on the surface of discontinuous objects. Since the noises and unwrapping errors are always localized at the projection blind spots, an algorithm is designed to determine the blind spots automatically with the light intensity difference information. Besides, in order to improve the measurement accuracy, a processing scheme is introduced to deal with the local height distortion introduced by the dual-frequency grating profilometry. Lots of measurement tests on various surfaces are carried out to assess the optimized profilometry, and experimental results indicate that the modified profilometry system works more robust with high reliability and accuracy in measuring different kinds of surfaces, especially discontinuous ones.

Keywords: Three-dimensional profilometry, automatic determination of blind spots, measurement of discontinuous surfaces, local height distortion correction.

1. INTRODUCTION

With the development of science and industrial production, there has been a growing need for three-dimensional profilometry in automated inspection, cultural creativity, biomedicine, heritage, etc. [1]. With the proficiency of full-field analysis, non-contact, and high precision profilometry based on fringe projection has become one of the most essential and popular branches of active optical measurement [2]-[9].

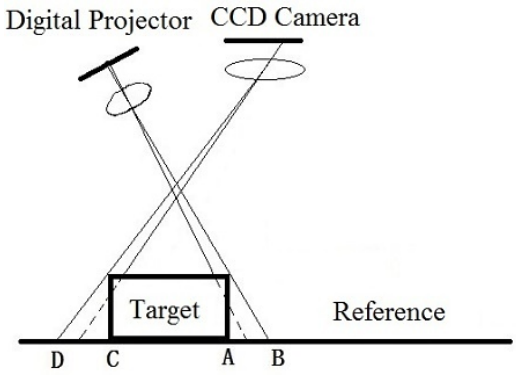

Fig.1. Illustration of a profilometry system.

A fringe projection profilometry system is usually composed of a projector, a camera, and a measurement target on a reference plane, as shown in Fig.1. There are two main methods to extract phase from the distorted fringes in fringe projection profilometry, phase-shifting profilometry (PSP) [3]-[5], and Fourier transform profilometry (FTP) [10]-[13]. Generally, FTP employs a single frame to evaluate the phases, whereas PSP needs at least three, FTP is thus much faster than PSP. However, with more sampling information, PSP is more accurate than FTP. Aiming at profilometry of various types of surfaces with high accuracy, PSP is selected here for further study.

The fundamental principle of PSP is extracting the relation between object surface height information and deformed fringes modulated by the object surface in a cycle. In general, the more deformed fringes are used, the higher the recovery accuracy will be. 4 fringes per cycle are taken in this paper. In measurement schemes suitable for discontinuous surfaces, the most crucial challenge is phase unwrapping [14]-[17]. In fact, wild fluctuations always lead to unwrapping error in conventional methods. To overcome this limitation, Saldner and Huntley et al. have proposed a time phase unwrapping algorithm. The method is based on projecting fringes of different frequencies to the surface of the measured object to

DOI: 10.2478/msr-2021-0027

obtain a plurality of deformed fringes modulated by the surface. Then the surface is restored by independently expanding the phases of each point in sequence. The time phase unwrapping method avoids the error spreading in principle [15]. Since then, the method has been the subject of several studies, aimed at improving its performance. Coggrave has proposed a fitted negative exponential growth sequence, which improved the measurement accuracy under the condition of taking the same number of images [16]. Huimin Qiu has introduced the dual-frequency grating projection measurement technology. However, the method requires a large amount of data: 6 sets, each made of 4 frames are needed, making a total of 24 raster images. In turn, the need of a large amount of data and the long measurement period have been crucial factors that have limited further popularization of the method. Pengcheng Yao and Shaoyan Gai et al. have introduced a cooperative multi-connected convolutional neural network for phase unwrapping with high accuracy and robustness [18]. Yanzhao Liu proposed a high-speed real-time 3D measurement system with a monochromatic camera [19]. The 3D shape of the object with color texture is retrieved using only six monochromes in total. Zhoujie Wu introduced gray-coded light for projection to avoid the jump errors on the boundary of code words, which are mainly caused by defocusing and motion [20]. Most of these researches focus on the real-time performance and accuracy of measurement technology [21]-[22].

Limited research has been found for the measurement of discontinuous surfaces. As a matter of fact, discontinuous surfaces are most common in natural scenes. This paper focuses on measurement of the discontinuous objects. It firstly analyzes the causes of noise from the perspective of light path and puts forward a solution to correct the noises and unwrapping errors from projection blind spots. Then, in further measurement experiments on more discontinuous planes, a processing scheme is proposed to deal with local height distortion to achieve high precision measurement of discontinuous surfaces.

The proposed technique was used to acquire the height value of tea tree surfaces for robotic tea plucking, and will be further explored in more fields of precision agriculture / forestry. Since tea tree surface is a typical discontinuous surface, the measurement of tea tree is one of the most challenging scenarios for our research.

2. BLIND SPOTS CORRECTION FOR PSP

At first, three sets of objects with regular shapes were chosen as measurement targets. PSP profilometry was used in the experiments, and results are shown in Fig.2. Fig.2.d), Fig.2.e), and Fig.2.f) are the measurement results of Fig.2.a), Fig.2.b), and Fig.2.c), respectively. In order to better illustrate results of the traditional method, the absolute height of the measurement surface has been normalized and linearly mapped to the pixel space of 0~255. Larger pixel values correspond to higher heights, and the highest point of the entire surface is mapped to pixel 255.

Some randomly distributed vertical pull lines occurred after the phase unwrapping. The isolated noises in the wrapped phase map were more concentrated in the shadow area, and the vertical pull line in the unwrapped phase map directly affected the final recovery, especially in Fig.2.e), where pull lines nearly covered the entire measurement object. From the direction of phase unwrapping, these pull lines tend to start in the shaded area and extend to the end.

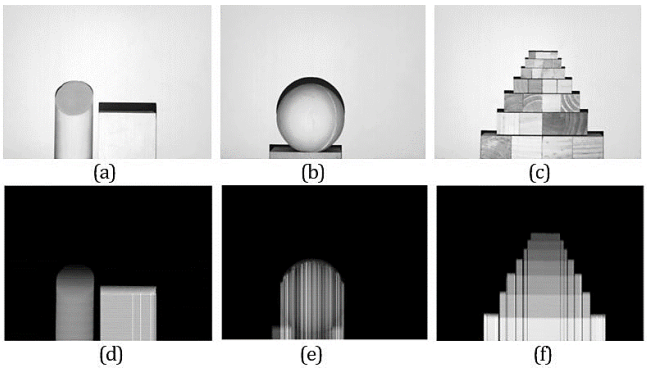

Fig.2. Measurement experiments based on PSP: a) beveled cylinder & cube, b) sphere, c) a plurality of standard cubes, d) recovery of beveled cylinder & cube, e) recovery of sphere, f) recovery of a plurality of standard cubes.

The "noise" in the shadow area may cause the error in phase unwrapping, and lead to distortion in the final restoration. Taking the experiment in Fig.2.a) as an example, the final measurement results show that the beveled cylinder is well restored, while the errors mainly appear in the shaded area under the projection beam. Fig.3.a) shows the wrapped phase distribution during the measurement, and the shadow area marked by the red box is shown enlarged in Fig.3.b) for a more detailed observation. The noises mostly appear in the shadow area. As the phase unwrapping, noises in the shaded area lead to "pull lines" in the unwrapping direction, which last to the end, as shown in Fig.3.c).

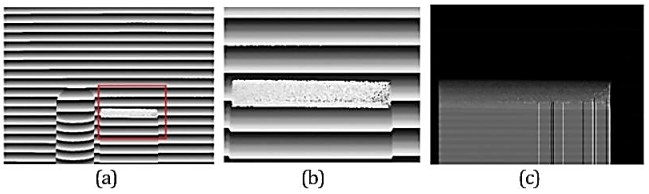

Fig.3. Unwrapping process description: a) distribution of wrapped phase and details, b) enlarged display of the shadow area marked by the red box, c) enlarged display of the shadow area in the unwrapped distribution.

It would be clearer to analyze the measurement scheme from the perspective of the optical structure, as shown in Fig.1. The experiments were conducted in a slanted projection system where the shooting direction was perpendicular to the reference plane. The triangular structure formed by the reference plane, the projection direction, and the shooting direction is the theoretical basis of the profilometry system based on fringe projection. However, blind spots do exist due to this triangular relationship. Blind spots are divided into projection blind and shooting blind according to the diverse ways of the formation. The

projection blind spot, as shown in Fig.1. from point A to B, is due to the block in optical path of projection, such that the shadow area cannot be projected by the grating stripes. Similarly, the shooting blind spot, as shown from point C to D, is obscured by an object in the optical path to camera lens, which makes the details behind the shelter unreachable. Once the position of the measured object and the projection or acquisition device reach a particular angle, a blind spot would appear, especially when the surface of the measured objects has lots of ups and downs. Since 3D profilometry is based on the image processing of the deformed fringes, the shooting blind area, which cannot be seen by the camera, cannot be measured by the system. On the other hand, the projection blind spots can be collected by the camera, and affect the accuracy of the results.

Since the projection blind spots cannot be avoided in actual measurement, the pixel value in these regions would be mainly affected by the ambient light, and the final acquired light intensity values in these regions are relatively irregular compared to other normal areas where grating fringes are projected. This is the reason behind the appearance of randomly distributed noises in the projection shadow area.

Self-determination by light intensity difference is proposed in this paper to deal with the projection blind spots and improve the accuracy and reliability of actual measurement. Fig.5. displays the distribution of Column 500 of each shifted image from Fig.4., captured from the measurement. It is easy to figure out two characteristics of light intensity distribution by comparing the pixels from blind spots with the rest. The light intensity values in blind spots are lower than other parts, as shown in Fig.5. from 500th to 540th pixels. Besides, the difference between maximum and minimum values at the same shadow point of four shifted patterns is significantly smaller than non-shadow points, due to the change of light intensity from the shifted grating projection.

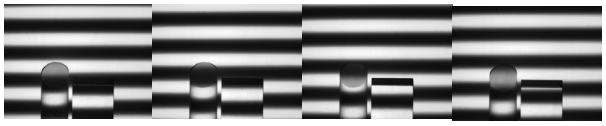

Fig.4. Deformed fringe patterns from the measuring surface.

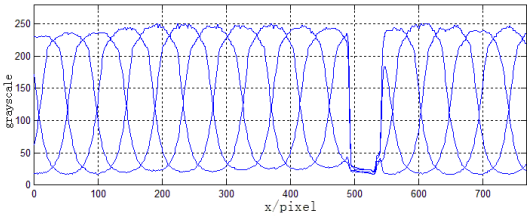

Fig.5. Contrast and analysis of light intensity.

The self-determination by light intensity difference method is designed and proposed according to the above analysis. At first, the maximum and minimum light intensity values of each pixel were obtained by comparing the four deformed fringes. Afterwards, the difference distribution between the two was calculated, as well as the average value of the whole difference distribution. 1/3 of the average value was adopted as a threshold value and used to scan the entire difference map accordingly. If the value is smaller than the threshold value, the point will be considered as a projection blind spot. Fig.6. shows the processing of the first set of experimental data. The average value of the difference map is 210, which means the threshold value is 70. Fig.6.d) shows the distribution of the maximum light intensity (upper dashed line), the minimum light intensity (lower dotted line), and the light intensity difference (solid line) from Column 500. The whole difference map was scanned to derive the location of projection blind spots. The determination result is shown in Fig.6.e), where the projection blind spots are marked with a pixel value of 255. After obtaining the position of projection blind spots, simply replace the package phase in blind spots with the value from the reference plane, and then unwrap the phase. This method could effectively eliminate the impact of projection blind spot, and improve accuracy.

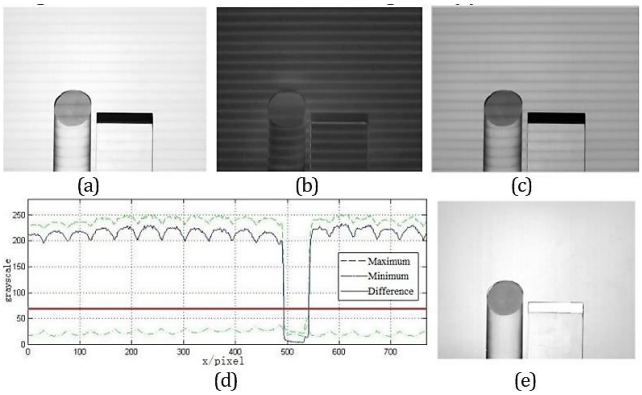

Fig.6. Processing of self-determination by intensity difference: a) maximum light intensity distribution, b) minimum light intensity distribution, c) light intensity difference distribution, d) light intensity difference from Column 500, e) blind spots marked with pixel 255.

The threshold to individuate the projection blind spots is worth further explanation. Through the analysis of Fig.6.d), it can be found that as long as the threshold is set within a certain range, the purpose of distinguishing the projection blind zone can be satisfied. The discrimination threshold of the 500th column can be set to any value between 25 and 190. However, in actual tests, it was found that the optional area of the threshold should be further narrowed due to the influence of the ambient light and the object reflection on the surface. The threshold at 1/3 of the average value of the light intensity difference map has been determined after analyzing a lot of experiments on different surfaces. Feasibility has been verified in subsequent experiments, and part of the test results are shown in section 4.2. In actual engineering practice, this parameter can be treated as a configurable parameter. The lower the threshold, the smaller areas will be judged as blind spots, and the probability of noise and error will be higher. Conversely, higher threshold value would result in more false blind spots, and in such case, multiple measurements are required.

Other experiments have been carried out to assess the self-determination method for blind spots based on light intensity

difference. Fig.7. shows the recoveries of the three groups of subjects. The abnormal noises in the projection blind spots have been basically eliminated and no vertical pull lines were generated.

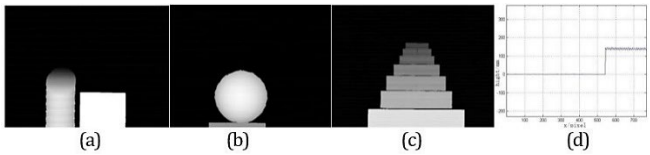

Fig.7. Experiment results of optimized measurement: recovery of beveled cylinder & cube a), sphere b), a plurality of standard cubes c), and d) data of column 500 in the recovery of beveled cylinder & cube.

3. MULTI-STEP SELECTION FILTERING FOR DUAL-FREQUENCY PROJECTION

After further observation of the recoveries in Fig.7., it was found that there are certain height fluctuations in the flat part of the surface, implying that the accuracy of recovery is low. As shown in Fig.7.d), after reaching the cube outer surface at the 540th pixel, the height value fluctuates up and down around 140 mm. This low accuracy and large fluctuations are not only caused by the non-sinusoidal features of the projection grating and the non-linearity of the entire measurement system, but also by the low projection grating frequency. This issue has already been analyzed through two aspects [23]-[25]: taking a compensation algorithm to correct the system error and increasing the projection grating frequency to improve the measurement accuracy, thereby reducing the amplitude of the wave. However, high frequency measurements would lead to insufficient sampling within a cycle, which may cause unwrapping errors in the result. To solve this problem, this paper adopts a dual-frequency grating projection method, which improves systematic measurement accuracy and, at the same time, avoids phase expansion errors. The low frequency part is exploited to detect the contours, whereas the high frequency part is useful to detect the details.

Experiments have been carried out on recoveries of the three groups of subjects using dual-frequency profilometry, with low-frequency at 16 cycles (48 pixels/period) and high-frequency at 64 cycles (12 pixels/period). Self-determination of blind spots has been employed to determine the blind spots and avoid the noises in the processing. The recoveries are shown in Fig.8. The fluctuations are largely reduced, and the accuracy has been largely improved.

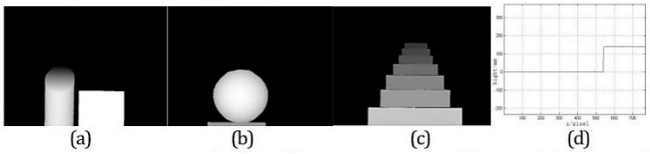

Fig.8. Experiment results of dual-frequency grating profilometry: recovery of beveled cylinder & cube a), sphere b), standard cubes c), and d) data of column 500 in the recovery of beveled cylinder & cube.

However, when the measurement results are displayed as a three-dimensional diagram, Fig.9., some mutated pixels show up. Because of the complexity of actual measurements, and the occurrence of noise, surface mutations, etc., there are always some errors in the final recovery. According to the unwrapping theory of dual-frequency projection, errors in the unwrapping of high-frequency components do not lead to spatial "pull lines", so they are not easy to detect in the two-dimensional display. However, these dead pixels do affect the accuracy of the final reconstruction.

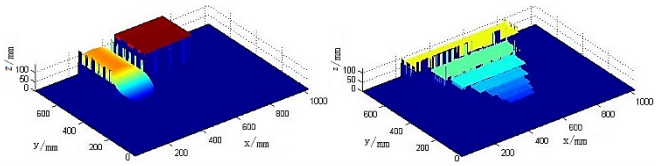

Fig.9. Mutation of height values in experimental results.

In this paper, three-dimensional profilometry is employed to acquire the height value of the tea tree surfaces for robotic tea plucking [26]-[30]. It is a difficult job since the intermittent tea tree surface is composed of irregularly shaped tea leaves. A similar plastic turf surface was used as measurement object, as shown in Fig.10.a). Dual-frequency profilometry with low-frequency at 16 cycles and high-frequency at 64 cycles was used with self-determination of blind spots. The result is shown in Fig.10.b). The general contour has been successfully restored, but in 3D, see Fig.10.c), some errors showed up like in Fig.9. The height distortion points are marked inside the ellipse mark. The result of the entire recovery is displayed after normalization in Fig.10.d), where we could see the distribution of abnormal points. They are randomly scattered in the whole graph, mostly gathered at the boundary of the projection blind area. These abnormal points are significantly higher than the original height by one or two cycles.

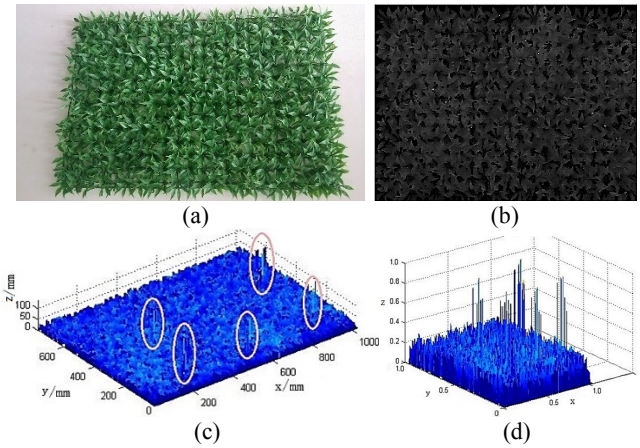

Fig.10. Measurement Experiment of artificial turf model: a) artificial turf model, b) recovery of turf in 2D, c) recovery of turf in 3D, d) normalized measuring results of artificial turf model.

This paper designs a processing scheme called multi-step selection filtering (MSF) based on the above analysis.

First, the height of measurement result from dual-frequency profilometry is normalized, and several thresholds are set according to the different situations of height mutation. Then, large connected areas above the threshold are removed to filter out the identification bits under these thresholds. Next, all the identification bits are overlaid as height mutation positions, which should be corrected. Finally, all the height mutation positions are processed with the modified median filtering.

As Fig.12. shows, modified median filtering is a scheme for fixing the located distortion pixels. It takes a similar median filter method to replace the identification bits with the median in the template, which expands from 3*3 to include each individual marked area. When a marked area is fully contained in the template, the mean height of non-marked points is calculated to replace the marked points.

The main processing flowchart of the multi-step selection filtering is shown in Fig.11., and Fig.12. displays the algorithm flow of the modified median filter method to replace the identification bits.

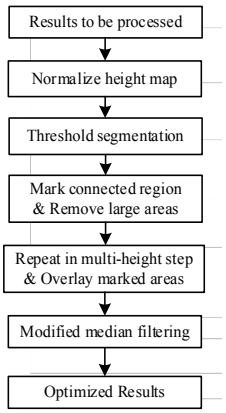

Fig.11. Multi-step filtering.

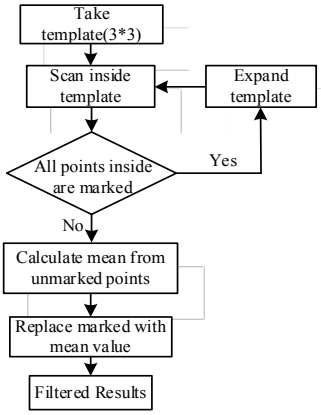

Fig.12. Modified median filtering.

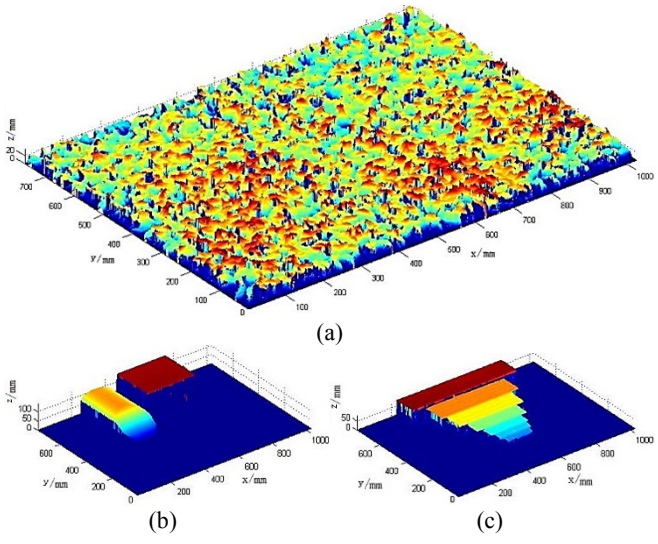

Fig.13. Optimized recoveries: a) turf, b) cylinder & cube, c) blocks.

In summary, MSF is a post-processing technique for correcting the local height mutations in the measurement results. Results of the three-dimensional measurement of plastic turf using the above optimization algorithm are shown in Fig.13. The multi-step selection filtering method has successfully removed the height mutation points. Fig.13. also shows the final measurement results of Cylinder cube and blocks using MSF, and it could effectively solve the height mutations problem.

4. RESULTS AND DISCUSSION

The overall flowchart of the modified profilometry proposed in this paper is shown in Fig.14.

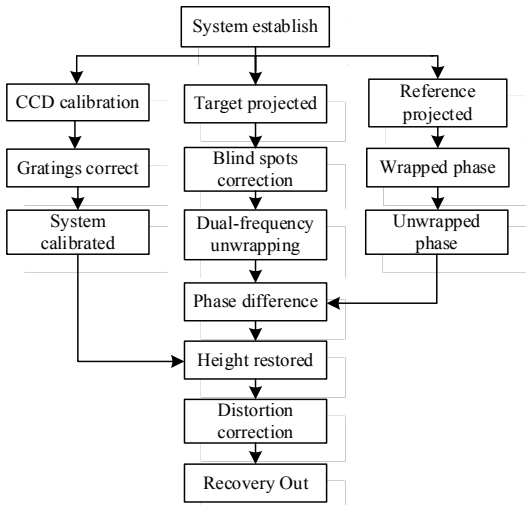

Fig.14. Overall flowchart of the modified profilometry.

4.1. Verification with discontinuous objects

To assess the reliability and accuracy of the proposed system, a well-designed discontinuous object composed of a plastic turf and a group of small cylinders with known height was used as test target. Fig.15.a) shows the well-designed discontinuous target. The 10 cylinders with known heights are randomly placed inside the discontinuous plastic turf.

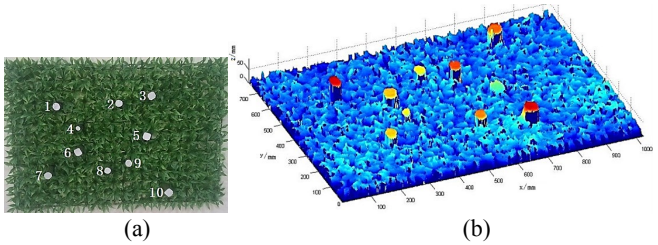

Fig.15. Experimental verification of highly discontinuous objects: a) 10 cylinders placed in turf, b) recovery of the target.

In the experiment, dual-frequency profilometry with self-determination of blind spots is used. After multi-step selection filtering, the measurement object is restored as shown in Fig.15.b). By comparing with measured objects, the method still has a reliable performance on the measurement of discontinuous objects. The accuracy is then checked by the

heights of the target cylinders. The height of the measured center point is directly compared with the height of the standard mark. Ten sets of data are shown in Table 1. The measurement error is within ± 1 m, and the error ratio does not exceed 2 %.

Table 1. Calibration results.

Index	Actual height (mm)	Recovery height (mm)	Error (mm)	Error ratio (%)
1	60	59.26	-0.74	1.23
2	64	64.97	0.97	1.52
3	80	79.81	-0.19	0.24
4	53	53.02	0.02	0.04
5	40	39.82	-0.18	0.45
6	60	59.07	-0.93	1.55
7	80	79.81	-0.19	0.24
8	55	55.30	0.30	0.55
9	70	69.83	-0.17	0.24
10	68	68.87	0.87	1.28

4.2. Verification with multiple objects

The measurement algorithm for discontinuous surfaces could be widely applied in more recovery of discontinuous objects. More experiments on a variety of different surface measurements have been carried out to verify the adaptability of the measurement system. Six typical measurement objects are shown in Fig.16., which are keyboard, mouse, fan impeller, iPad packaging box, mask, and sailboat model. The 3D recoveries are displayed in Fig.16.

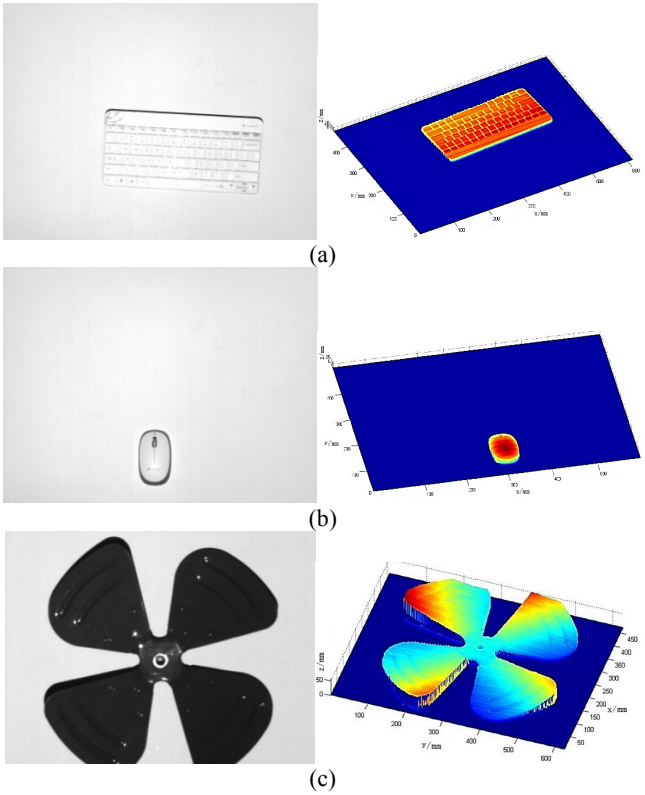

(a) (b) (c) (d) (e) (f)

Fig.16. Multiple measurement results in a three-dimensional map: a) keyboard, b) mouse, c) fan impeller, d) iPad packaging box, e) mask, f) sailboat model.

5. CONCLUSION

A three-dimensional profilometry system based on fringe projection has been built with a digital projector and a CCD camera. Experiments with objects having discontinuous surfaces have been carried out. The optimized profilometry has been proven able to recover various surfaces with raising complexity. Plus, it yielded high accuracy as well as sufficient reliability.

At first, phase shifting profilometry (PSP) has been selected for further research by comparing the simulation and experiment results of simple objects. Then, it was found that noises, discontinuities, and line-like errors were caused by the uncontrollable light intensity within the blind spots from the projection. A solution has been proposed using the difference of light intensity to determine the blind spots automatically. After being detected, the phase values would be replaced by the wrapped phase map of the reference plane from the same position.

A dual-frequency grating profilometry has been then used to improve the measurement accuracy. However, it led to some abnormal height values, which were caused by the phase unwrapping of high-frequency components. A processing scheme has been introduced to solve the problem. It consists in spotting the pixels with abnormal height values by considering features of height and area distribution, and then substituting the spots by modified median filtering.

Various measurement experiments have been performed on different surfaces, including regular planes, spherical surfaces, stairs, fan impeller, complex turf, and sailboat

model. The turf and the sailboat model are particularly challenging examples. Not only the shape is abnormally irregular, but also with a large number of truncations. Meanwhile, a quantifiable evaluation case for discontinuous surface measurement has been designed for the turf, shown in section 4.1, which has fully proved the effectiveness of the optimization method proposed in this paper. Moreover, the optimized 3D profilometry was used in field experiment for 3D positioning of tea tree surfaces in an automated platform for tea plucking, and can be further explored in more fields of agriculture and forestry research. There will surely be more challenges. In conclusion, the optimized profilometry can be used for the measurement of diverse types of surfaces with high accuracy.

ACKNOWLEDGMENT

This work was supported by Key Research and Development Program of Jiangsu Province (Grant No. BE2021016) and Jiangsu Agricultural Science and Technology Innovation Fund (Grant No. CX(21)3184).

REFERENCES

[1] Luhmann, T., Robson, S., Kyle, S., Harley, I. (2006). *Close Range Photogrammetry: Principles, Techniques and Applications*. Whittles, ISBN 9781870325509.

[2] Hyun, J.S., Zhang, S. (2020). Influence of projector pixel shape on ultrahigh-resolution 3D shape measurement. *Optics Express*, 28 (7), 9510-9520.

[3] Zhang, S. (2018). High-speed 3D shape measurement with structured light methods: A review. *Optics and Lasers in Engineering*, 106, 119-131.

[4] Qian, J., Feng, S., Li, Y., Tao, T., Han, J., Chen, Q., Zuo, C. (2020). Single-shot absolute 3D shape measurement with deep-learning-based color fringe projection profilometry. *Optics Letters*, 45 (7), 1842-1845.

[5] Zhou, P., Zhang, Y., Yu, Y., Cai, W., Zhou, G. (2020). 3D shape measurement based on structured light field imaging. *Mathematical Biosciences and Engineering*, 17 (1), 654-668.

[6] Zou, H., Da, F., Wang, Z. (2015). A novel 3D face feature based on Geometry image vertical shape information. *Optik*, 126 (9-10), 898-902.

[7] Huang, P.S., Zhang, S., Chiang, F.-P. (2005). Trapezoidal phase-shifting method for three-dimensional shape measurement. *Optical Engineering*, 44 (12), 123601.

[8] Quan, C., He, X., Tay, C.J., Shang, H.M. (2001). 3D surface profile measurement using LCD fringe projection. In *Second International Conference on Experimental Mechanics*. SPIE, vol. 4317.

[9] Karpinsky, N., Zhang, S. (2012). High-resolution, real-time 3D imaging with fringe analysis. *Journal of Real-Time Image Processing*, 71, 55-66.

[10] Takeda, M., Mutoh, K. (1983). Fourier transform profilometry for the automatic measurement of 3D object shape. *Applied Optics*, 22 (24), 3977-3982.

[11] Su, X., Chen, W. (2001). Fourier transform profilometry: A review. *Optics and Lasers in Engineering*, 35 (5), 263-284.

[12] Su, X., Chen, W., Zhang, Q., Chao, Y. (2001). Dynamic 3-D shape measurement method based on FTP. *Optics and Lasers in Engineering*, 36 (1), 49-64.

[13] Su, X., Su, L., Li, W., Xiang, L. (1998). New 3D profilometry based on modulation measurement. In *Automated Optical Inspection for Industry: Theory, Technology, and Applications II*. SPIE, vol. 3558.

[14] Goldstein, R.M., Zebker, H.A., Werner, C.L. (1988). Statellite radar interferometry: Two-dimensional phase unwrapping. *Radio Science*, 23 (4), 713-720.

[15] Huntley, J.M., Saldner, H. (1993). Temporal phase-unwrapping algorithm for automated interferogram analysis. *Applied Optics*, 32 (17), 3047-3052.

[16] Huntley, J.M., Coggrave, C.R. (1998). Progress in phase unwrapping. In *International Conference on Applied Optical Metrology*. SPIE, vol. 3407.

[17] Chan, P.H., Bryanston-Cross, P.J., Parker, S.C. (1995). Fringe-pattern analysis using a spatial phase-stepping method with automatic phase unwrapping. *Measurement Science and Technology*, 6, 1250-1259.

[18] Yao, P., Gai, S., Chen, Y., Chen, W., Da, F. (2021). A multi-code 3D measurement technique based on deep learning. *Optics and Lasers in Engineering*, 143, 106623.

[19] Liu, Y., Fu, Y., Zhou, P., Zhuan, Y., Zhong, K., Guan, B. (2020). A real-time 3D shape measurement with color texture using a monochromatic camera. *Optics Communications*, 474, 126088.

[20] Wu, Z., Guo, W., Li, Y., Liu, Y., Zhang, Q. (2020). High-speed and high-efficiency three-dimensional shape measurement based on Gray-coded light. *Photonics Research*, 8 (6), 819-829.

[21] Guo, W., Wu, Z., Li, Y., Liu, Y., Zhang, Q. (2020). Real-time 3D shape measurement with dual-frequency composite grating and motion-induced error reduction. *Optics Express*, 28 (18), 26882-26897.

[22] Zhang, J., Guo, W., Wu, Z., Zhang, Q. (2021). Three-dimensional shape measurement based on speckle-embedded fringe patterns and wrapped phase-to-height lookup table. *Optical Review*, 28, 227-238.

[23] Zhang, S., Yau, S.T. (2007). Generic nonsinusoidal phase error correction for three-dimensional shape measurement using a digital video projector. *Applied Optics*, 46 (1), 36-43.

[24] Hu, Y.S., Xi, J.T., Li, E.B., Chicharo, J., Yang, Z.K. (2006). Three-dimensional profilometry based on shift estimation of projected fringe patterns. *Applied Optics*, 45 (4), 678-687.

[25] Gai, S., Da, F. (2011). A novel fringe adaptation method for digital projector. *Optics and Lasers in Engineering*, 49 (4), 547-552.

[26] Jin, X., Chen, Y., Guo, Y., Sun, Y., Chen, J. (2013). Tea flushes identification based on machine vision for high-quality tea at harvest. *Applied Mechanics and Materials*, 288, 214-218.

[27] Jin, X., Chen, Y., Zhang, H., Sun, Y., Chen, J. (2012). High-quality tea flushes detection under natural conditions using computer vision. *International Journal of Digital Content Technology and its Applications (Gyeongju)*, 6 (8), 600-606.

[28] Zhang, H., Chen, Y., Wang, W., Zhang, G. (2014). Positioning method or tea picking using active computer vision. *Nongye Jixie Xuebao / Transactions of the Chinese Society of Agricultural Machinery*, 45 (9), 61-65.

[29] Jin, X., Che, J., Chen, Y. (2021). Weed identification using deep learning and image processing in vegetable plantation. *IEEE Access*, 9, 10940-10950.

[30] Jiang, H., Jiang, X., Ru, Y., Wang, J., Xu, L., Zhou, H. (2020). Application of hyperspectral imaging for detecting and visualizing leaf lard adulteration in minced pork. *Infrared Physics & Technology*, 110, 103467.

Received July 11, 2021
Accepted October 18, 2021